



Article

# Zn<sub>2</sub>SnO<sub>4</sub>@SiO<sub>2</sub>@5-FU Nanoparticles as an Additive for Maxillary Bone Defects

Ana Maria Gianina Rehner (Costache)<sup>1</sup>, Andreea Gabriela Bratu<sup>2</sup>, Alexandra Cătălina Bîrcă<sup>2</sup>,  
Adelina-Gabriela Niculescu<sup>2,3</sup> , Alina Maria Holban<sup>4</sup>, Ariana Hudiță<sup>3,4</sup> , Florentina Cornelia Bîclesanu<sup>1</sup>,  
Paul Cătălin Balaure<sup>2</sup> , Anna Maria Pangică<sup>1</sup>, Alexandru Mihai Grumezescu<sup>2,3,\*</sup>   
and George-Alexandru Croitoru<sup>5</sup>

<sup>1</sup> Faculty of Medicine, Titu Maiorescu University, 031593 Bucharest, Romania; rehner.ana@gmail.com (A.M.G.R.); corneliabicle@yahoo.com (F.C.B.); anna-maria.pangica@prof.utm.ro (A.M.P.)

<sup>2</sup> Faculty of Chemical Engineering and Biotechnologies, University Politehnica of Bucharest, Gh. Polizu St. 1-7, 060042 Bucharest, Romania; gabriela.bratu@stud.fim.upb.ro (A.G.B.); ada\_birca@yahoo.com (A.C.B.); adelina.niculescu@upb.ro (A.-G.N.); paul.balaure@upb.ro (P.C.B.)

<sup>3</sup> Research Institute of the University of Bucharest—ICUB, University of Bucharest, 050657 Bucharest, Romania; arianahudita@yahoo.com

<sup>4</sup> Faculty of Biology, University of Bucharest, Aleea Portocalelor 1-3, Sector 5, 77206 Bucharest, Romania; alina\_m\_h@yahoo.com

<sup>5</sup> Faculty of Dental Medicine, Carol Davila University of Medicine and Pharmacy, 8 Eroii Sanitari Street, 050474 Bucharest, Romania; alex.croitoru@umfcd.ro

\* Correspondence: agrumezescu@upb.ro

**Abstract:** This study investigates the synthesis of Zn<sub>2</sub>SnO<sub>4</sub>@SiO<sub>2</sub>@5-FU nanoparticles as an additive for bone fillers in dental maxillofacial reconstruction. Zn<sub>2</sub>SnO<sub>4</sub> nanoparticles were synthesized and coated with a SiO<sub>2</sub> shell, followed by the incorporation of 5-Fluorouracil (5-FU), aimed at enhancing the therapeutic properties of classical fillers. Structural analysis using X-ray diffraction confirmed that Zn<sub>2</sub>SnO<sub>4</sub> was the single crystalline phase present, with its crystallinity preserved after both SiO<sub>2</sub> coating and 5-FU incorporation. SEM characterization revealed the micro-spherical particles of Zn<sub>2</sub>SnO<sub>4</sub> assembled by an agglomeration of nanorods, exhibiting dimensions and morphological characteristics that were consistent after the addition of both the SiO<sub>2</sub> shell and 5-FU. Fourier-transformed infrared spectroscopy provided solid proof of the successful synthesis of Zn<sub>2</sub>SnO<sub>4</sub>, Zn<sub>2</sub>SnO<sub>4</sub>@SiO<sub>2</sub>, and Zn<sub>2</sub>SnO<sub>4</sub>@SiO<sub>2</sub>@5-FU, confirming the presence of expected functional groups. The SiO<sub>2</sub> layer improved nanoparticle stability in the solution, as indicated by zeta potential measurements, while adding 5-FU significantly increased biocompatibility and targeting efficiency. The existence of the SiO<sub>2</sub> shell and 5-FU is also confirmed by the hydrodynamic diameter, indicating an increase in particle size after incorporating both compounds. Antibacterial assays demonstrated a selective efficacy against Gram-positive bacteria, with Zn<sub>2</sub>SnO<sub>4</sub>@SiO<sub>2</sub>@5-FU showing the strongest inhibitory effects. Biofilm inhibition studies further confirmed the nanoparticles' effectiveness in preventing bacterial colonization. Cytotoxicity tests on the A-431 human epidermoid carcinoma cell line revealed a dose-dependent reduction in cell viability, highlighting the potential of 5-FU for targeted cancer treatment. These findings highlight the potential of Zn<sub>2</sub>SnO<sub>4</sub>@SiO<sub>2</sub>@5-FU nanoparticles as a multifunctional additive for bone fillers, offering enhanced antimicrobial and antitumor capabilities.

**Keywords:** Zn<sub>2</sub>SnO<sub>4</sub> nanoparticles; SiO<sub>2</sub> coating; 5-Fluorouracil; antibacterial activity; antitumor therapy; nanoparticle stability; biofilm inhibition; A-431 cell line; drug delivery; biomedical applications



Academic Editor: Maciej Monedeiro-Milanowski

Received: 3 December 2024

Revised: 24 December 2024

Accepted: 27 December 2024

Published: 29 December 2024

**Citation:** Rehner, A.M.G.; Bratu, A.G.; Bîrcă, A.C.; Niculescu, A.-G.; Holban, A.M.; Hudiță, A.; Bîclesanu, F.C.; Balaure, P.C.; Pangică, A.M.; Grumezescu, A.M.; et al.

Zn<sub>2</sub>SnO<sub>4</sub>@SiO<sub>2</sub>@5-FU Nanoparticles as an Additive for Maxillary Bone Defects. *Int. J. Mol. Sci.* **2025**, *26*, 194. <https://doi.org/10.3390/ijms26010194>

**Copyright:** © 2024 by the authors. Licensee MDPI, Basel, Switzerland. This article is an open access article distributed under the terms and conditions of the Creative Commons Attribution (CC BY) license (<https://creativecommons.org/licenses/by/4.0/>).

## 1. Introduction

Bone fillers are critical in dental maxillofacial reconstruction, aiding in restoring and integrating bone structures that have been compromised due to injury, disease, or surgical procedures [1]. Dental maxillofacial bone repair involves irregular anatomy, equilibrium between hosts and oral cavity microbes, and advanced periodontal structures that promote epithelial growth. Consequently, oral maxillofacial reconstruction needs replacement materials that meet rigorous and precise standards [2–4]. Biocompatible materials are crucial in conventional treatments because of the specific requirements for advancements in clinical therapy and tissue regeneration [5,6]. Despite the advancements in biomaterials, traditional bone fillers face challenges such as the risk of infection, inadequate integration with host tissue, and limited stability. Unfortunately, the conventional clinical therapies for maxillofacial tumors (radiotherapy, chemotherapy, and surgery) are harmful to the host, leading to insufficient therapeutic results such as physiological limitations, including difficulties with speech, swallowing, chewing, sucking, and breathing, as well as tumor recurrence. At the same time, dental materials may stimulate immunological responses, resulting in inflammation or rejection, leading to tissue fibrosis growth and the resorption of the alveolar bone [7,8]. There is a growing need for bone fillers that support bone regeneration and exhibit antimicrobial and antitumor properties to enhance treatment outcomes [9].

Nanotechnology has emerged as a promising approach in dental and medical applications, offering unique advantages in terms of size, structure, surface area, and bioactivity [10]. Bone substitutes are classified as bone grafts (autograft, allograft, and xenograft), ceramics/synthetics (hydroxyapatite and tricalcium phosphate), and growth factors (human demineralized bone matrix) [11–13]. Autologous bone grafting was once considered the gold standard for bone filling, providing all characteristics for bone regeneration: osteoinductivity, osteoconductivity, and osteogenicity. However, the limitations of donors have restricted its development. Exogenous bone replacement materials are susceptible to immune reactions and disease transmission, and artificial material grafts make it challenging to achieve optimal therapeutic results due to their lack of osteogenic induction characteristics [8,14,15]. Incorporating nanomaterials into bone fillers can significantly improve their mechanical properties, enhance bone regeneration, support and regulate cellular function, proliferation, and migration, and provide effective antimicrobial activity. These benefits make nanoparticles ideal candidates for advanced biomedical applications, particularly in enhancing bone filler performance in dental maxillofacial reconstruction [16–19].

$Zn_2SnO_4$  belongs to the class of ternary oxides, which possess remarkable characteristics and can be synthesized in different morphologies. These nanoparticles have garnered attention due to their distinctive properties, including high crystallinity, non-toxicity, chemical stability, antioxidant properties, pH-dependent properties, optical properties, sustained release of zinc ions, and potential antimicrobial capabilities [20–24]. Specifically,  $Zn_2SnO_4$  nanoparticles exhibit a higher availability of reactive oxygen species (ROS) than similar nanosystems (i.e., ZnO and  $SnO_2$  nanoparticles), leading to enhanced antibacterial activity. Moreover,  $Zn^{2+}/Sn^{4+}$  ions released from  $Zn_2SnO_4$  are attracted to the negatively charged bacterial cell membrane. These ions penetrate the membrane, interact with sulfhydryl groups in membrane proteins, and disrupt enzymatic activity, including synthetase function. This interference hampers cell division, ultimately causing bacterial cell death [20,25]. These characteristics make  $Zn_2SnO_4$  an attractive material for biomedical applications displaying excellent antibacterial properties toward relevant pathogens [22,26–28]. Thus, these nanomaterials can be of interest for enhancing bone fillers' structural and antimicrobial properties by interacting with microbial cell membranes.

Furthermore, zinc stannate can display an antitumoral effect by raising the levels of ROS inside the malignant cell, and, eventually, oxidative stress damages the constituents of the cell. Antitumor effects have been noted to be dose-dependent, with higher  $\text{Zn}_2\text{SnO}_4$  nanoparticle concentrations providing elevated intracellular ROS levels in exposed cancer cells. The oxidative damage has been further linked with a reduction in cancer cell migration and proliferation, with a significant decrease in metastasis risks [20–24]. Moreover,  $\text{Zn}_2\text{SnO}_4$  nanoparticles can be functionalized for improved tumor cell targeting and internalization [29], holding promise as theranostic tools. In this context, the development of  $\text{Zn}_2\text{SnO}_4$ -based nanomaterials could address the limitations of conventional bone fillers, providing a multifunctional solution for complex dental reconstructions.

To further improve the performance of  $\text{Zn}_2\text{SnO}_4$  nanoparticles, surface modifications were employed using a  $\text{SiO}_2$  shell and 5-Fluorouracil (5-FU). The  $\text{SiO}_2$  coating enhances the stability and dispersibility of the nanoparticles in solution [30,31], while 5-FU, a known chemotherapeutic and antibacterial agent, introduces supplementary antitumor and antimicrobial properties [32–35]. This dual modification aims to create a multifunctional nanoparticle that can facilitate bone regeneration, prevent infections, and potentially target tumor cells, making it suitable for use in dental maxillofacial applications.

The primary objective of this study is to develop multifunctional  $\text{Zn}_2\text{SnO}_4@ \text{SiO}_2@ 5\text{-FU}$  nanoparticles as an additive for bone fillers in dental maxillofacial reconstruction. This work aims to evaluate the structural integrity, biocompatibility, antimicrobial efficacy, and antitumor potential of these modified nanoparticles. By addressing the limitations of existing bone fillers, this research seeks to contribute to developing more effective materials for reconstructive dental applications.

## 2. Results

### 2.1. X-Ray Diffraction Spectrum (XRD)

The phase purity and crystallinity of  $\text{Zn}_2\text{SnO}_4$  nanoparticles were characterized using X-ray Diffraction (XRD) analysis, as illustrated in Figure 1. The XRD pattern confirms that the nanoparticles exhibit a single-phase structure, specifically  $\text{Zn}_2\text{SnO}_4$ , with no evidence of secondary phases such as  $\text{SnO}_2$ ,  $\text{ZnO}$ , or  $\text{ZnSnO}_3$ . All the observed diffraction peaks align with the Fd-3m cubic-spinel structure typical of  $\text{Zn}_2\text{SnO}_4$ . Notable high-intensity diffraction peaks are observed at approximately  $17.775^\circ$ ,  $29.17^\circ$ ,  $35.177^\circ$ ,  $41.682^\circ$ , and  $60.505^\circ$ . According to the reference data from the PDF and ICDD (International Centre for Diffraction Data) sheets, these peaks correspond to the (111), (311), (222), (400), and (440) planes, all characteristic of a cubic crystal system. The average crystallite size of the synthesized  $\text{Zn}_2\text{SnO}_4$  nanoparticles was determined using the Debye–Scherrer equation (Equation (1)), yielding an estimated size of approximately 191.508 Å:

$$D = \frac{K \times \lambda}{\beta \times \cos \theta} \quad (1)$$

where

D = average grain size (nm);

K = Scherrer constant, which denotes the shape of the particle and has the value of 0.9;

$\lambda$  = X-ray wavelength (1.54184 Å);

$\beta$  = full-width at half-maximum of the observed peaks (FWHM);

$\theta$  = diffraction angle ( $^\circ$ ).

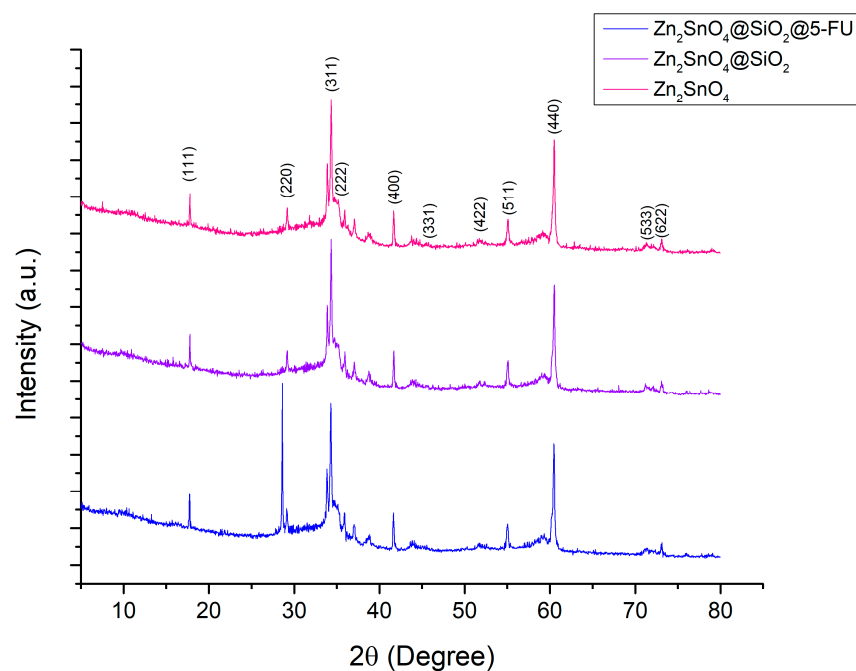


**Figure 1.** XRD patterns of  $\text{Zn}_2\text{SnO}_4$ ,  $\text{Zn}_2\text{SnO}_4@SiO_2$ , and  $\text{Zn}_2\text{SnO}_4@SiO_2@5-FU$  samples.

Table 1 presents the average crystallite size values obtained for  $\text{Zn}_2\text{SnO}_4$ ,  $\text{Zn}_2\text{SnO}_4@SiO_2$ , and  $\text{Zn}_2\text{SnO}_4@SiO_2@5-FU$  nanoparticles.

**Table 1.** The average crystallite size of  $\text{Zn}_2\text{SnO}_4$ -based nanoparticles.

Sample	$\text{Zn}_2\text{SnO}_4$	$\text{Zn}_2\text{SnO}_4@SiO_2$	$\text{Zn}_2\text{SnO}_4@SiO_2@5-FU$
Average crystallite size (Å)	191.508	217.575	209.065

Figure 1 presents the X-ray diffraction patterns for the synthesized samples. In the  $\text{Zn}_2\text{SnO}_4@SiO_2$  and  $\text{Zn}_2\text{SnO}_4@SiO_2@5-FU$  samples, a slight shift in the diffraction peaks is noticeable, which can be attributed to the  $SiO_2$  coating on the particles. Additionally, the peak intensities exhibit a moderate reduction compared to the pure  $\text{Zn}_2\text{SnO}_4$  sample, indicating a decrease in crystallinity for the  $\text{Zn}_2\text{SnO}_4@SiO_2$  and  $\text{Zn}_2\text{SnO}_4@SiO_2@5-FU$  samples. This observation confirms that the  $\text{Zn}_2\text{SnO}_4$  nanoparticles were successfully encapsulated with  $SiO_2$  and subsequently with 5-FU. The XRD pattern of  $\text{Zn}_2\text{SnO}_4@SiO_2@5-FU$  presents an intense peak at  $28.603^\circ$ , characteristic of the crystalline nature of 5-FU.

## 2.2. Scanning Electron Microscopy (SEM)

SEM micrographs reveal that the  $\text{Zn}_2\text{SnO}_4$  particles exhibit a spherical morphology formed by the aggregation of nanorods, as depicted in Figure 2 at magnifications of  $25,000\times$  and  $50,000\times$ . These particles demonstrate a tendency to agglomerate and display dimensional uniformity, suggesting a high level of homogeneity in shape. Dimensional analysis was conducted for both spherical and rod-like morphologies, with average particle sizes of 1.17, 1.28, and 1.44  $\mu\text{m}$  for spherical particles and 94.5, 114.68, and 106.48 nm for the nanorods. Following the  $SiO_2$  coating, a shell layer becomes visible on the surface of the particles, as shown in the micrographs in Figure 3. With the subsequent incorporation of 5-FU, the coating layer appears even more defined, as indicated in Figure 4. This suggests that 5-FU interacts with the silica shell, potentially forming a denser and more uniform layer around the particles. Notably, adding the silica shell and 5-FU does not significantly impact the size or morphology of the original  $\text{Zn}_2\text{SnO}_4$  particles, indicating that the coating and drug incorporation processes preserve the physical dimensions and

shape. Figure 5 illustrates the size distribution for both spherical particles and the nanorod-aggregated spheres.

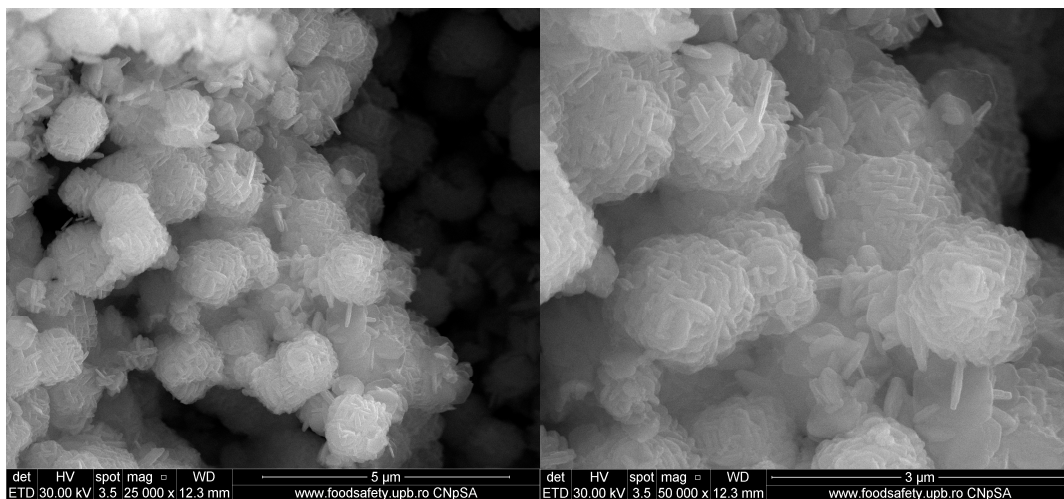


Figure 2. SEM micrographs of  $Zn_2SnO_4$ .

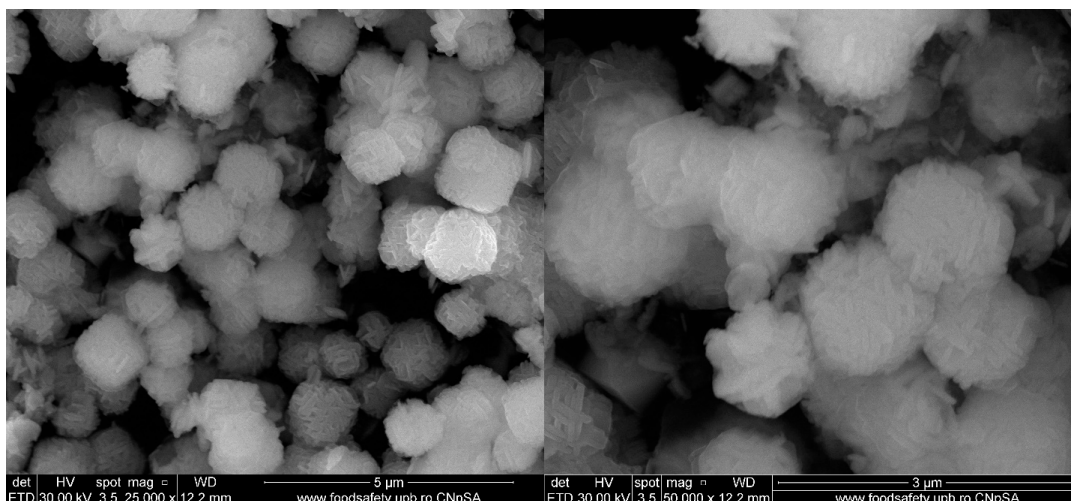


Figure 3. SEM micrographs of  $Zn_2SnO_4@SiO_2$ .

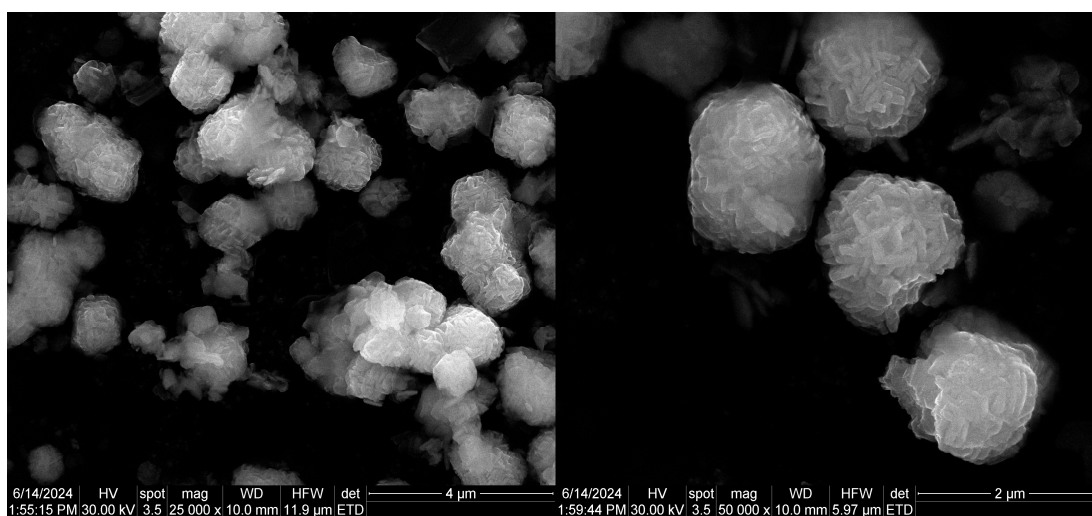
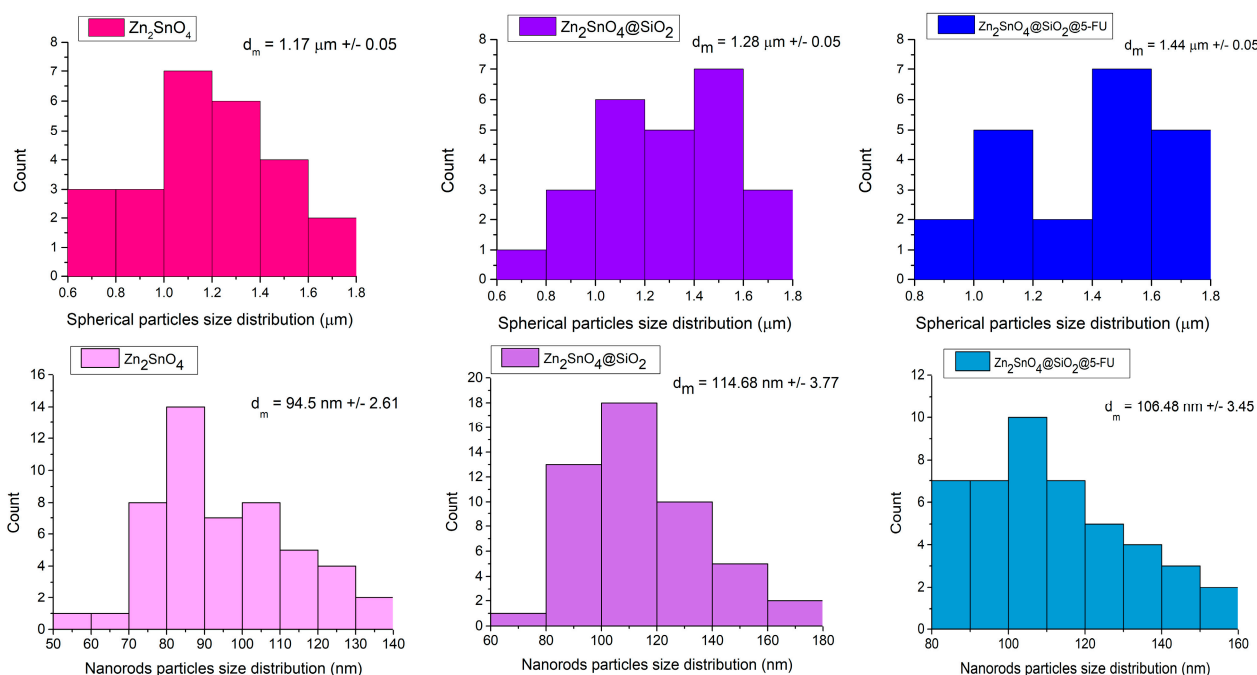


Figure 4. SEM micrographs of  $Zn_2SnO_4@SiO_2@5-FU$ .



**Figure 5.** Particle size distribution of spheres ( $\mu\text{m}$ ) and nanorods (nm), as computed from the corresponding SEM micrograph of each material. Size measurements were performed using ImageJ software V 1.53, analyzing multiple images to ensure accuracy and reproducibility.

### 2.3. Energy Dispersive Spectroscopy (EDS)

SEM characterization is frequently complemented by energy-dispersive X-ray spectroscopy (EDS), which includes elemental mapping to visually distinguish the presence of each element within the samples. For Zn<sub>2</sub>SnO<sub>4</sub>@SiO<sub>2</sub>, the elemental mapping reveals the presence of O, Si, Sn, and Zn, with each element represented by distinct colors, confirming the sample's composition. The EDS spectra, illustrated in Figure 6, corroborate these findings by displaying characteristic peaks for each detected element. The mapping results indicate a uniform distribution of all elements across the sample. The Zn<sub>2</sub>SnO<sub>4</sub>@SiO<sub>2</sub>@5-FU sample underwent similar analysis, yielding comparable results regarding elemental composition. EDS mapping identified O, Si, Sn, and Zn, each highlighted in distinct colors in Figure 7. Additionally, the EDS spectra confirm that the inclusion of 5-FU does not alter the elemental composition, maintaining consistent characteristics as observed in the Zn<sub>2</sub>SnO<sub>4</sub>@SiO<sub>2</sub> sample. Additionally, the EDS spectra confirm that the inclusion of 5-FU does not alter the elemental composition, maintaining consistent characteristics with the Zn<sub>2</sub>SnO<sub>4</sub>@SiO<sub>2</sub> sample. This observation, combined with FTIR analysis, suggests that 5-FU is primarily physically adsorbed onto the Zn<sub>2</sub>SnO<sub>4</sub>@SiO<sub>2</sub> surface without forming new chemical bonds.

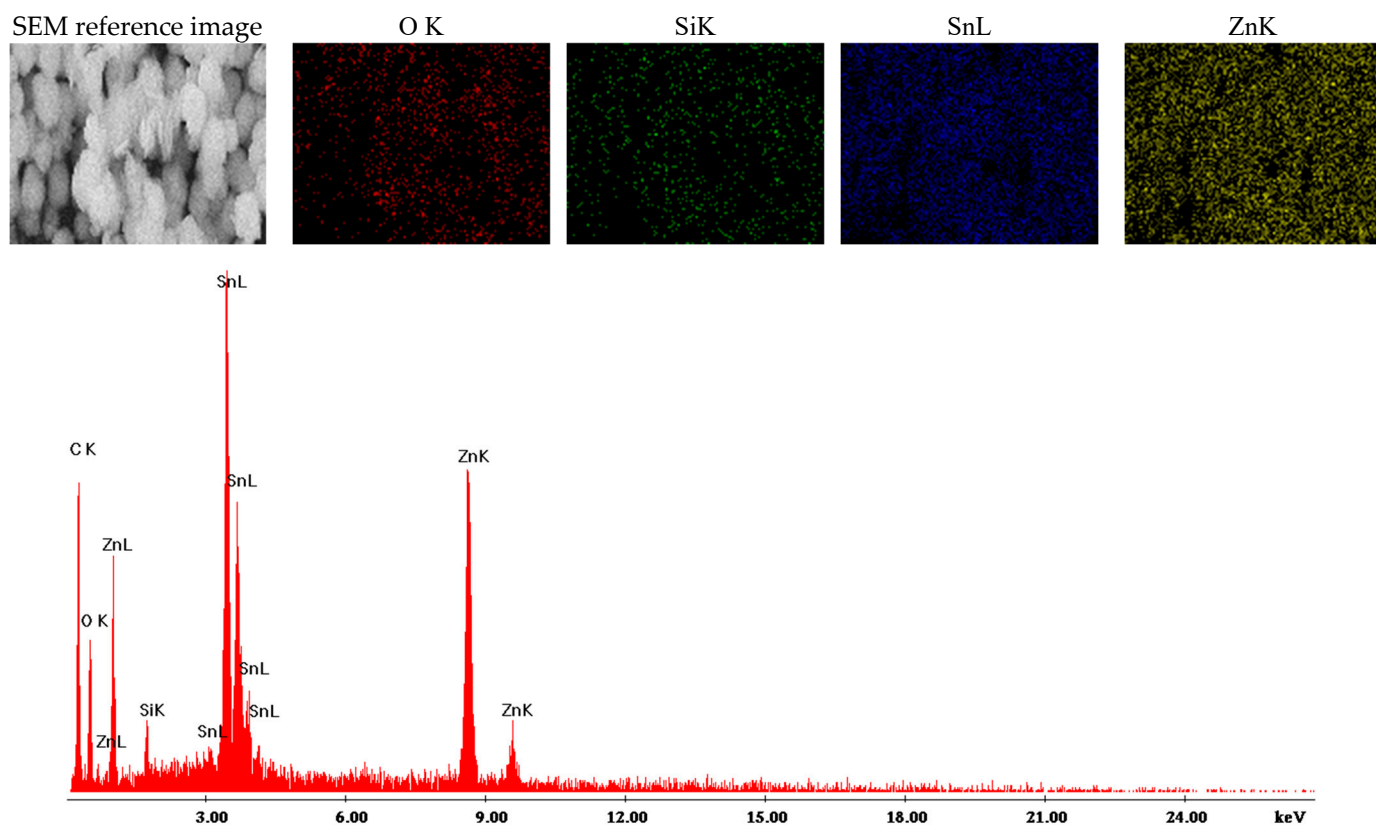


Figure 6. Elemental mapping obtained for  $Zn_2SnO_4@SiO_2$ .

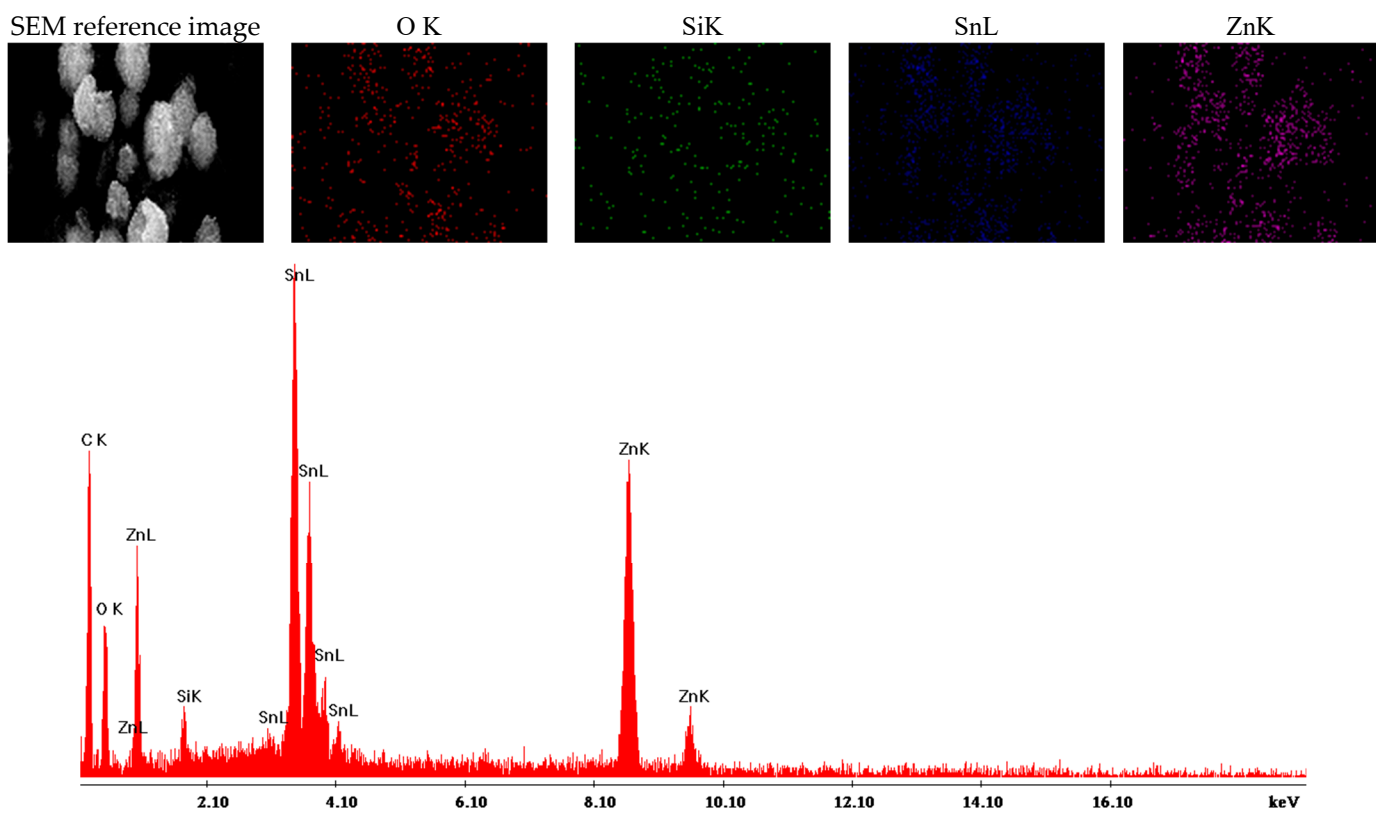
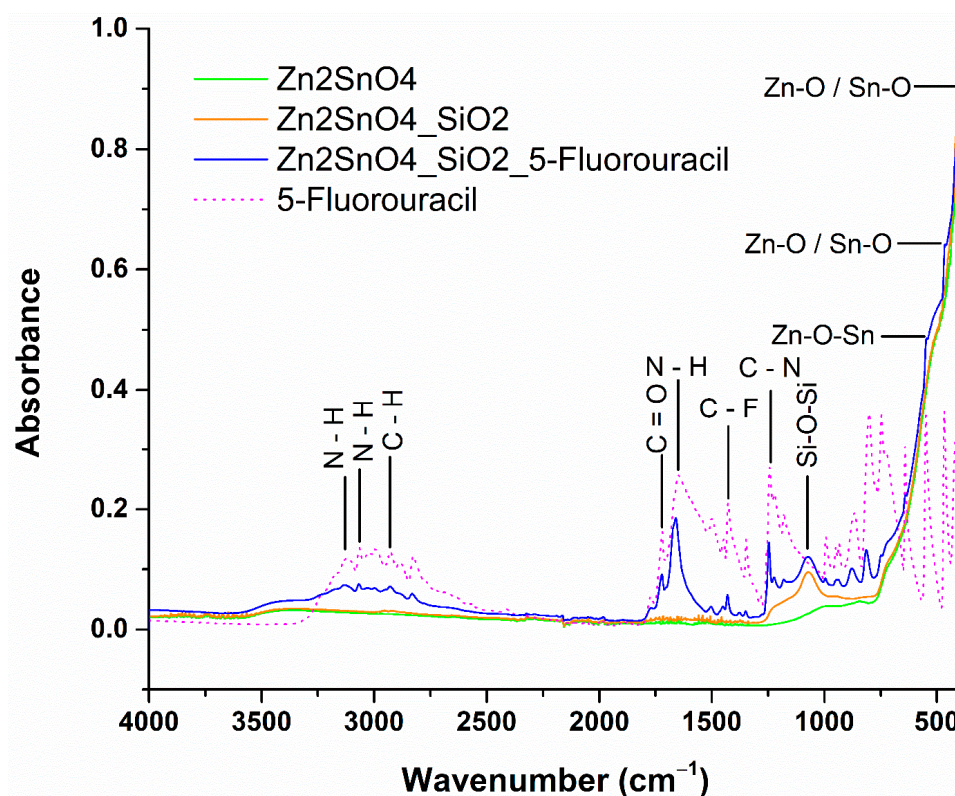


Figure 7. Elemental mapping obtained for  $Zn_2SnO_4@SiO_2@5-FU$ .

#### 2.4. Fourier Transform Infrared Spectroscopy (FTIR)

Valuable insights into the vibrational characteristics of atomic bonds within the material can be gained through Fourier Transform Infrared (FTIR) analysis. Measurements for all powder samples were conducted over a wavenumber range of 400 to 4000  $\text{cm}^{-1}$ . The resulting FTIR spectra, which provide information on the functional groups and bonding present in the samples, are illustrated in Figure 8.



**Figure 8.** FTIR spectra results for  $\text{Zn}_2\text{SnO}_4$ ,  $\text{Zn}_2\text{SnO}_4@\text{SiO}_2$ ,  $\text{Zn}_2\text{SnO}_4@\text{SiO}_2@5\text{-FU}$ , and 5-FU substance.

The FTIR analysis of the zinc stannate sample reveals a prominent vibrational band at 590  $\text{cm}^{-1}$ , which corresponds to the symmetric stretching vibration of ZnO and SnO<sub>2</sub> groups, indicating the Zn–O–Sn bonding characteristic of  $\text{Zn}_2\text{SnO}_4$ . This absorption band strongly supports the successful formation of the zinc stannate compound, which is consistent with its expected properties. Additionally, wavenumbers at 463  $\text{cm}^{-1}$  and 400  $\text{cm}^{-1}$  are attributed to Zn–O and Sn–O chemical groups, respectively, confirming the synthesis of zinc stannate. These vibrational bands are consistently observed in all the synthesized samples, indicating that zinc stannate is the primary constituent in the formulations [36,37]. For  $\text{Zn}_2\text{SnO}_4@\text{SiO}_2$  and  $\text{Zn}_2\text{SnO}_4@\text{SiO}_2@5\text{-FU}$  samples, a distinct vibrational band at 1072  $\text{cm}^{-1}$  is observed, corresponding to the Si–O–Si functional group, which confirms the presence of the SiO<sub>2</sub> coating layer. The incorporation of 5-FU in the  $\text{Zn}_2\text{SnO}_4@\text{SiO}_2@5\text{-FU}$  structure is validated by several absorption bands in the FTIR spectra, consistent with the reference spectrum for 5-FU. Notably, N–H bending vibrations are detected at 3130 and 3067  $\text{cm}^{-1}$ , along with a similar bending band at 1600  $\text{cm}^{-1}$ , characteristic of the 5-FU compound. Additionally, C–H stretching appears at 2929  $\text{cm}^{-1}$ , while the C=O functional group is identified at 1772  $\text{cm}^{-1}$ . Strong evidence for 5-FU integration is further provided by the stretching vibration at 1430  $\text{cm}^{-1}$ , attributed to the fluoro compound C–F, and a band at 1240  $\text{cm}^{-1}$  associated with the C–N functional group [38,39].

### 2.5. Dynamic Light Scattering (DLS)

Zeta potential measurements highlight that  $\text{Zn}_2\text{SnO}_4$  nanoparticles possess a negatively charged surface, with an average value of  $-17.93$  mV, indicating superior stability in solution. The negative surface charge not only ensures dispersion stability but also enhances their potential for interacting with biological membranes, including both bacterial and cancer cells. These interactions are key to the nanoparticles' antimicrobial and cytotoxic effects. The addition of a  $\text{SiO}_2$  layer enhances the stability of the samples in solution, forming a protective shell around the  $\text{Zn}_2\text{SnO}_4$  nanoparticles. This is reflected in a zeta potential measurement of approximately  $-21.45$  mV for the  $\text{Zn}_2\text{SnO}_4@ \text{SiO}_2$  sample. The silica coating helps to prevent nanoparticle aggregation and sedimentation, ensuring even dispersion within the solution.

Furthermore, incorporating 5-FU onto the nanoparticles' surface further increases stability, resulting in a zeta potential of  $-51.15$  mV. This significant increase in stability is attributed to the interaction between 5-FU and the silica shell, leading to a highly stable solution, as depicted in Figure 9. The enhanced negative zeta potential also correlates with the observed antimicrobial and antitumor effects as the negatively charged nanoparticles strongly interact with positively charged regions of bacterial and cancer cell membranes. This facilitates membrane disruption, increased oxidative stress, and improved drug delivery efficiency, leading to heightened antibacterial and anticancer activity. Such enhanced stability is useful for medical applications, ensuring that the nanoparticles remain structurally intact and functionally effective until they reach their target site within the body.

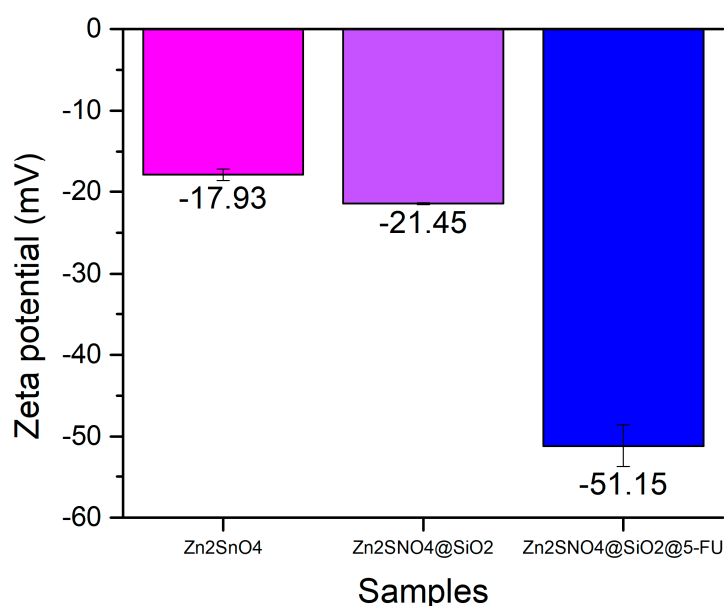


**Figure 9.** Zeta potential (mV) results of  $\text{Zn}_2\text{SnO}_4$ ,  $\text{Zn}_2\text{SnO}_4@ \text{SiO}_2$ , and  $\text{Zn}_2\text{SnO}_4@ \text{SiO}_2@ 5\text{-FU}$  samples.

The hydrodynamic diameter measurements confirm that the particle size increased following the addition of both  $\text{SiO}_2$  and 5-FU, indicating successful coverage with the silica shell and the subsequent incorporation of the antitumoral and antibacterial agent. For the uncoated  $\text{Zn}_2\text{SnO}_4$  nanoparticles, the hydrodynamic diameter was estimated to be 1636.83 nm. Upon coating with  $\text{SiO}_2$ , the hydrodynamic diameter increased to approximately 1839.06 nm, demonstrating the successful formation of the silica layer around the  $\text{Zn}_2\text{SnO}_4$  nanoparticles.

Furthermore, after the integration of 5-FU, the dynamic light scattering (DLS) results showed similar hydrodynamic diameter characteristics to those of the  $\text{Zn}_2\text{SnO}_4@ \text{SiO}_2$  sample, suggesting that 5-FU was uniformly incorporated into the  $\text{SiO}_2$  surface (Figure 10).

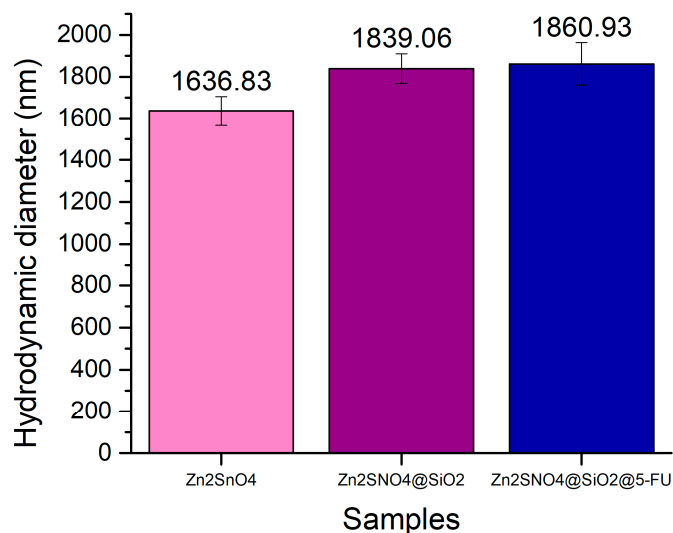


**Figure 10.** Hydrodynamic diameter (nm) results of Zn<sub>2</sub>SnO<sub>4</sub>, Zn<sub>2</sub>SnO<sub>4</sub>@SiO<sub>2</sub>, and Zn<sub>2</sub>SnO<sub>4</sub>@SiO<sub>2</sub>@5-FU samples.

### 2.6. Antimicrobial Assay

The MIC values presented in Figure 11 reveal the antibacterial performance of the Zn<sub>2</sub>SnO<sub>4</sub>-based nanoparticles against *S. aureus* (Gram-positive) and *E. coli* (Gram-negative). Against both *S. aureus* and *E. coli*, the Zn<sub>2</sub>SnO<sub>4</sub>@SiO<sub>2</sub>@5-FU formulation demonstrates the lowest MIC, indicating the highest antibacterial efficacy among the tested samples. This result highlights the contribution of 5-FU functionalization, which enhances the antimicrobial activity through its chemotherapeutic and antibacterial properties. However, the Zn<sub>2</sub>SnO<sub>4</sub>@SiO<sub>2</sub> formulation shows a slightly reduced antibacterial activity compared to Zn<sub>2</sub>SnO<sub>4</sub>, likely due to the silica shell partially shielding the core and reducing the availability of active species such as ROS and Zn<sup>2+</sup>/Sn<sup>4+</sup> ions, which are essential for antimicrobial efficacy.

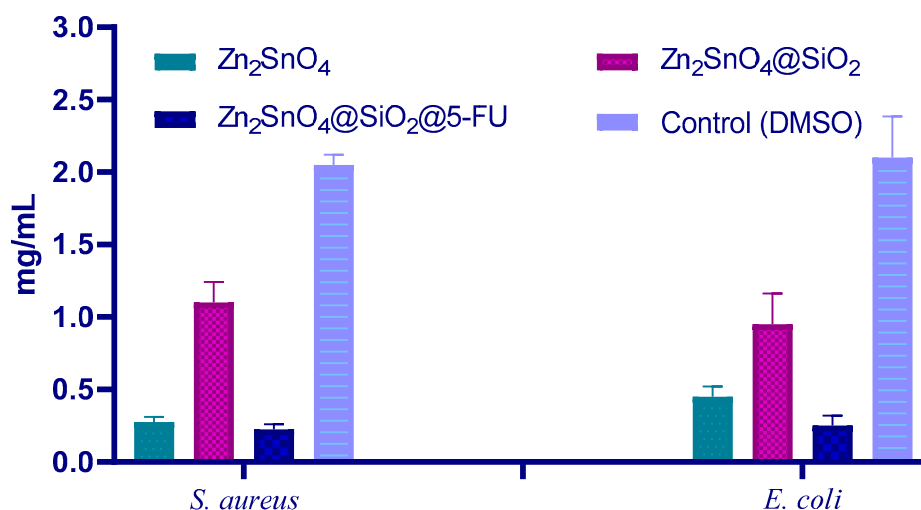


**Figure 11.** The minimum inhibitory concentration (MIC) of Zn<sub>2</sub>SnO<sub>4</sub>, Zn<sub>2</sub>SnO<sub>4</sub>@SiO<sub>2</sub>, and Zn<sub>2</sub>SnO<sub>4</sub>@SiO<sub>2</sub>@5-FU samples against *S. aureus* and *E. coli*.

The MIC results for *E. coli* are comparable to those observed for *S. aureus*, suggesting that the formulations are equally effective against both bacterial types despite the structural differences between Gram-positive and Gram-negative bacteria. The enhanced efficacy of Zn<sub>2</sub>SnO<sub>4</sub>@SiO<sub>2</sub>@5-FU across both strains underscores the potential of this multifunctional nanoparticle system for broad-spectrum antibacterial applications. The DMSO control

demonstrates significantly higher MIC values, confirming that the observed antibacterial effects are attributable to the nanoparticle formulations. These findings suggest that  $\text{Zn}_2\text{SnO}_4@\text{SiO}_2@5\text{-FU}$  is a promising antibacterial agent with efficacy against both Gram-positive and Gram-negative bacteria.

The antimicrobial mechanism of  $\text{Zn}_2\text{SnO}_4@\text{SiO}_2@5\text{-FU}$  nanoparticles against Gram-positive and Gram-negative bacteria can be attributed to their distinct structural and functional features. For Gram-positive bacteria such as *S. aureus*, the thick and porous peptidoglycan layer facilitates the penetration of nanoparticles and their active species. Reactive oxygen species generated by  $\text{Zn}_2\text{SnO}_4$  nanoparticles interact with bacterial cell walls, proteins, and DNA, inducing oxidative stress, which disrupts vital cellular processes [20,24]. Additionally, the release of  $\text{Zn}^{2+}$  and  $\text{Sn}^{4+}$  ions interferes with bacterial enzymatic activities by binding to sulfhydryl (-SH) groups in membrane proteins, destabilizing the membrane and impairing metabolic pathways [23,28]. These processes, combined with the antimicrobial properties of 5-FU, enhance membrane disruption and lead to bacterial lysis, contributing to the observed efficacy against Gram-positive strains [40].

In Gram-negative bacteria like *E. coli*, the presence of an outer membrane composed of lipopolysaccharides serves as a protective barrier, making these bacteria inherently more resistant to antimicrobial agents [41]. However, the  $\text{Zn}_2\text{SnO}_4@\text{SiO}_2@5\text{-FU}$  nanoparticles overcome this barrier through multiple mechanisms. ROS produced by the nanoparticles penetrate the outer membrane and cause oxidative damage [20,24], while  $\text{Zn}^{2+}$  and  $\text{Sn}^{4+}$  ions interact with negatively charged LPS molecules, destabilizing the outer membrane and increasing permeability [28,41]. This enables the nanoparticles and 5-FU to access the thinner peptidoglycan layer and the underlying cellular components. The incorporation of 5-FU further disrupts bacterial DNA synthesis and metabolic pathways, amplifying the overall antimicrobial effect [40,42]. These synergistic mechanisms allow  $\text{Zn}_2\text{SnO}_4@\text{SiO}_2@5\text{-FU}$  nanoparticles to achieve comparable efficacy against both Gram-positive and Gram-negative bacteria, showcasing their potential as broad-spectrum antibacterial agents [42].

### 2.7. Cytotoxicity Assay

To evaluate the cytotoxicity activity of  $\text{Zn}_2\text{SnO}_4$ ,  $\text{Zn}_2\text{SnO}_4@\text{SiO}_2$ , and  $\text{Zn}_2\text{SnO}_4@\text{SiO}_2@5\text{-FU}$  powders on the A-431 human epidermoid carcinoma cell line, cells were treated for 24 h with varying concentrations of these nanoparticles. Post-treatment cell metabolic activity was assessed using the MTT spectrophotometric assay to determine the cytotoxicity of each powder on A-431 tumor cells.

The cytotoxicity assessment (Figure 12) revealed that all  $\text{Zn}_2\text{SnO}_4$ -based powders exerted a toxic effect on A-431 tumor cells, with the cytotoxicity increasing in a dose-dependent manner. While all three powders significantly reduced cell viability at both high and low concentrations, a marked decrease in cell viability was observed at concentrations as low as 37.5  $\mu\text{g}/\text{mL}$ . At a 1.5  $\mu\text{g}/\text{mL}$  concentration, no significant cytotoxic effect was detected compared to the untreated control across all samples. Despite similarities in their cytotoxic profiles,  $\text{Zn}_2\text{SnO}_4@\text{SiO}_2@5\text{-FU}$  exhibited the strongest cytotoxicity, causing a more pronounced decrease in cell viability than  $\text{Zn}_2\text{SnO}_4$  and  $\text{Zn}_2\text{SnO}_4@\text{SiO}_2$  at equivalent concentrations. At the highest concentration tested (1  $\text{mg}/\text{mL}$ ),  $\text{Zn}_2\text{SnO}_4$  reduced cell viability by a factor of 1.9 compared to the control,  $\text{Zn}_2\text{SnO}_4@\text{SiO}_2$  by 2.75 times, and  $\text{Zn}_2\text{SnO}_4@\text{SiO}_2@5\text{-FU}$  by 3.45 times, with significant cytotoxicity also observed at lower treatment concentrations.

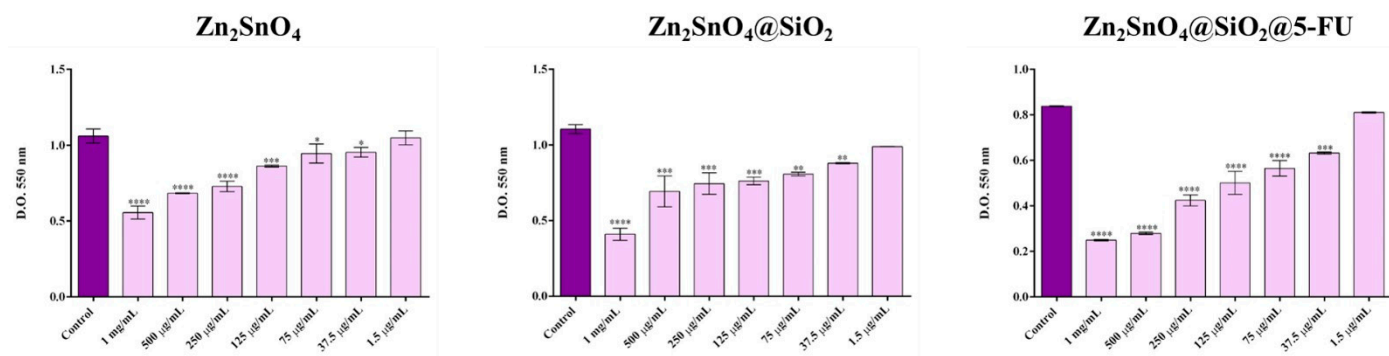


**Figure 12.** Graphics representing the viability of A-431 tumor cells after 24 h post-treatment with different concentrations of  $\text{Zn}_2\text{SnO}_4$ ,  $\text{Zn}_2\text{SnO}_4@\text{SiO}_2$ , and  $\text{Zn}_2\text{SnO}_4@\text{SiO}_2@5\text{-FU}$  powders (\*\*\*\*  $p \leq 0.0001$  control vs. sample, \*\*\*  $p \leq 0.001$  control vs. sample, \*\*  $p \leq 0.01$  control vs. sample, and \*  $p \leq 0.05$  control vs. sample).

Furthermore, the cytotoxicity data were utilized to estimate the lethal dose 50 ( $\text{LD}_{50}$ )—the concentration required to kill 50% of the cells exposed. The  $\text{LD}_{50}$  for  $\text{Zn}_2\text{SnO}_4$  was 1 mg/mL, while the  $\text{LD}_{50}$  for  $\text{Zn}_2\text{SnO}_4@\text{SiO}_2$  could not be precisely determined but fell between 500 µg/mL and 1 mg/mL. In contrast, the  $\text{LD}_{50}$  for  $\text{Zn}_2\text{SnO}_4@\text{SiO}_2@5\text{-FU}$  was 250 µg/mL, indicating a significantly higher cytotoxic potential for the 5-FU-incorporated sample due to the lower  $\text{LD}_{50}$  value.

Fluorescence microscopy, using the Live/Dead staining of A-431 tumor cells, confirmed the MTT assay findings (Figure 13). The  $\text{Zn}_2\text{SnO}_4$  powder displayed mild cytotoxic effects compared to the control. In the  $\text{Zn}_2\text{SnO}_4@\text{SiO}_2$  treatment, a noticeable decline in cell viability was observed, with cells losing their characteristic compact cluster formation, which is typical for tumor cell organization. The  $\text{Zn}_2\text{SnO}_4@\text{SiO}_2@5\text{-FU}$  powder, particularly at higher concentrations (1 mg/mL), showed the most substantial cytotoxic impact, with significantly fewer viable cells, which were organized into small, dispersed clusters, in stark contrast to the untreated control sample.

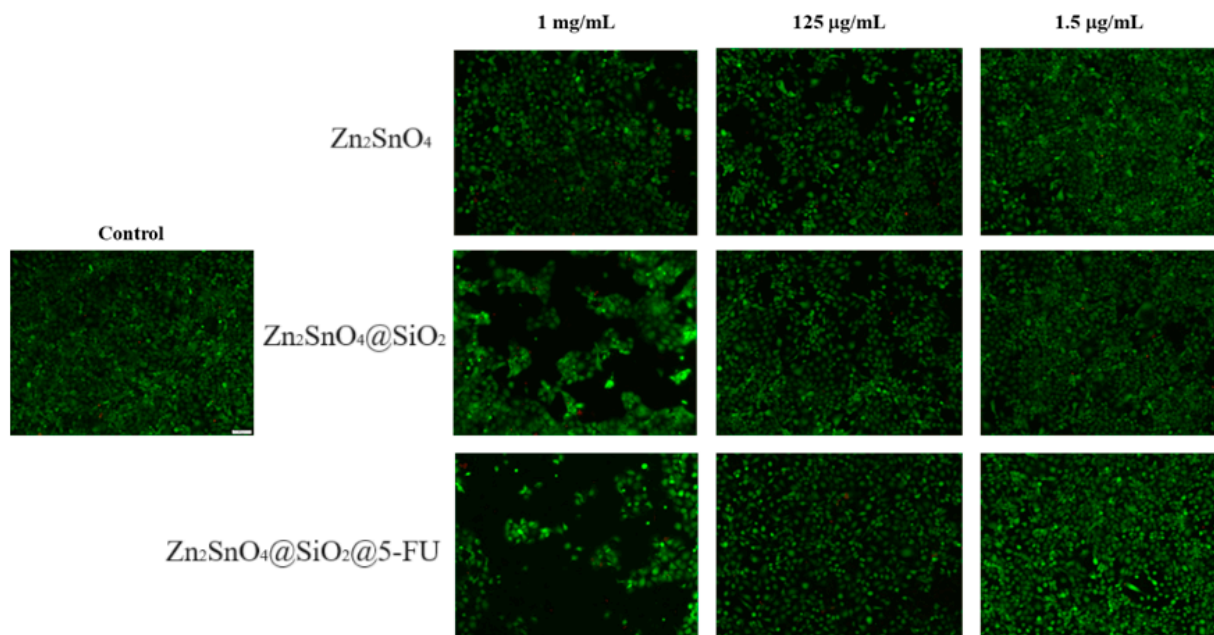


**Figure 13.** Fluorescence microscopy images showing living (green) and dead (red) A-431 tumor cells after 24 h post-treatment with different concentrations of  $\text{Zn}_2\text{SnO}_4$ ,  $\text{Zn}_2\text{SnO}_4@\text{SiO}_2$ , and  $\text{Zn}_2\text{SnO}_4@\text{SiO}_2@5\text{-FU}$  powders (10× magnification).

### 3. Discussion

Traditional bone fillers commonly used in dental maxillofacial reconstruction often include materials such as calcium phosphate cement, hydroxyapatite, and bioactive glass [43,44]. While these materials provide basic support for bone regeneration, they frequently exhibit limitations such as brittleness, fragility, a high rate of deterioration that impacts cell growth, susceptibility to infection, poor integration with host bone, and limited antimicrobial or antitumor capabilities. Structural and biocompatibility concerns, particularly the lack of effective barriers against microbial contamination and inadequate mechanical stability in the implanted bone fracture, remain major drawbacks in conventional fillers [45]. To increase the limited biodegradability and antibacterial action of the bone fillers, metal oxides such as MgO, ZnO, and ZrO<sub>2</sub> have been used [46–50]. The synthesized Zn<sub>2</sub>SnO<sub>4</sub>@SiO<sub>2</sub>@5-FU nanoparticles demonstrate clear advantages over traditional fillers regarding structural stability and biocompatibility. The presence of a SiO<sub>2</sub> coating significantly improves stability and dispersibility, addressing common issues of aggregation seen in conventional materials. SiO<sub>2</sub> is an inorganic compound suitable for coating over inner core materials because of its superior thermal stability, capacity to tolerate high temperatures, and protection against core deterioration in an acidic environment. S. Lims et al. used SiO<sub>2</sub> as a protective shell over Zn<sub>2</sub>SnO<sub>4</sub> nanoparticles, modifying their functionality and reactivity, which improves the stability of the inner core and prevents the aggregation of core particles. The Stöber method employed to cover the synthesized Zn<sub>2</sub>SnO<sub>4</sub> nanoparticles has several significant benefits, including high purity, environmental friendliness, and the simplicity of controlling shape and size [51,52].

Furthermore, Zn<sub>2</sub>SnO<sub>4</sub>@SiO<sub>2</sub>@5-FU nanoparticles offer enhanced integration potential due to their high biocompatibility and targeted functionalities, which are not found in standard bone fillers. Infection remains a critical concern in dental reconstructions using traditional fillers, which often lack intrinsic antibacterial properties. In contrast, Zn<sub>2</sub>SnO<sub>4</sub>@SiO<sub>2</sub>@5-FU nanoparticles display superior antibacterial activity, particularly against Gram-positive bacteria such as *S. aureus*. Y. Lakshmi et al. [28] reported the antibacterial activity of Zn<sub>2</sub>SnO<sub>4</sub> nanoparticles against Gram-positive bacteria (*B. subtilis* and *S. aureus*) and Gram-negative bacteria (*P. aeruginosa* and *E. coli*). The results indicate a significant antibacterial effect against both strains at higher concentrations (10 mg/L) [17].

The incorporation of 5-FU enhances this effect, offering a significant advantage in reducing post-surgical infection risks. The interaction between the SiO<sub>2</sub> and 5-FU was analyzed in numerous studies. C. Ding et al. presented that the dispersion of SiO<sub>2</sub> nanoparticles in hydrogels can increase the resistance of 5-FU release into the surrounding liquid and considerably lower the burst release [53]. In this context, Zn<sub>2</sub>SnO<sub>4</sub>@SiO<sub>2</sub>@5-FU represents a more reliable choice for maintaining sterile conditions in clinical applications. Biofilm formation is a major limitation of conventional bone fillers, often leading to persistent infections and compromised surgical outcomes. 5-FU exhibits antibacterial properties against *Streptococcus suis*, *Staphylococcus aureus*, and *E. coli*. In *Pseudomonas aeruginosa* and *E. coli*, it can lessen bacterial pathogenicity and prevent the growth of biofilms [40,42,54]. In this study, the Zn<sub>2</sub>SnO<sub>4</sub>@SiO<sub>2</sub>@5-FU nanoparticles showed notable efficacy in inhibiting biofilm formation, a feature that directly addresses the shortcomings of standard fillers. This capability is crucial for long-term clinical success as it ensures that the material maintains a sterile environment, preventing bacterial colonization and related complications. Unlike conventional bone fillers, Zn<sub>2</sub>SnO<sub>4</sub>@SiO<sub>2</sub>@5-FU nanoparticles possess distinct antitumor properties due to the inclusion of 5-FU, a chemotherapeutic agent. This dual functionality enables the filler to contribute to bone regeneration and the local treatment of cancerous tissues, which is particularly relevant in oral cancer contexts. A study showed that 5-FU can increase programmed death-ligand 1 (PD-L1) expression in a cell model of oral squamous

cell carcinoma, influencing treatment response and aiding chemoresistance [55]. In another research study, SiO<sub>2</sub> nanoparticles functionalized with chitosan and PEG and loaded with 5-FU demonstrated favorable uptake in cancer cell lines. Forty-eight-hour exposure treatments resulted in strong, induced cytotoxic, apoptotic, and cell-cycle distribution shift events in colon, breast, and cervical cancer cells that experienced rapid apoptotic events and cell-cycle distribution shifts. Furthermore, at therapeutically relevant dosages (0.15–0.18 mg<sub>5-FU</sub>/mg<sub>SiO<sub>2</sub></sub>), cytotoxicity studies demonstrated an effective reduction in the malignant cell population [56]. The ability to combine bone healing with targeted tumor therapy offers a unique advantage in complex dental reconstructions involving oncological concerns. The Zn<sub>2</sub>SnO<sub>4</sub>@SiO<sub>2</sub>@5-FU nanoparticles exhibit superior mechanical stability under the conditions expected in dental applications. This resilience surpasses that of many conventional fillers, which often suffer from structural weaknesses [41]. The enhanced mechanical properties of Zn<sub>2</sub>SnO<sub>4</sub>@SiO<sub>2</sub>@5-FU contribute to better bone regeneration and integration, leading to more robust and lasting outcomes in maxillofacial reconstructions. By promoting mineral formation at the bonded dentin/restoration interface and lessening the effects of acid-producing bacteria, these nanoparticles can increase dental restorations' strength and fatigue resistance [57]. Despite the advantages, potential challenges remain in the synthesis and use of Zn<sub>2</sub>SnO<sub>4</sub>@SiO<sub>2</sub>@5-FU. The functionalization processes employed in order to be environmentally compatible [58] are more complex than those required for standard fillers, which could impact scalability and clinical adoption. However, the enhanced therapeutic benefits justify these complexities, and further refinement could optimize the material for broader clinical use. Future studies should also consider potential cytotoxic effects at varying doses to ensure safety. Looking forward, *in vivo* studies will be critical to validate the performance of Zn<sub>2</sub>SnO<sub>4</sub>@SiO<sub>2</sub>@5-FU nanoparticles in real clinical scenarios. Additionally, combining these nanoparticles with other bioactive materials could amplify their efficacy, particularly in complex reconstructions. These developments can potentially revolutionize the field of dental and maxillofacial surgery, offering a more comprehensive solution to bone regeneration and infection prevention in reconstructive applications.

## 4. Materials and Methods

### 4.1. Materials

The materials used for the synthesis of Zn<sub>2</sub>SnO<sub>4</sub> nanoparticles included zinc nitrate (Zn(NO<sub>3</sub>)<sub>2</sub>·6H<sub>2</sub>O), tin tetrachloride (SnCl<sub>4</sub>), sodium hydroxide (NaOH), and distilled water. The SiO<sub>2</sub> shell was formed using ammonia (NH<sub>3</sub>) solution and tetraethyl orthosilicate (TEOS). Surface modification of the SiO<sub>2</sub> shell was achieved using 5-Fluorouracil (5-FU), which was attached through hydrogen bonding and Van der Waals interactions. All chemicals were sourced from Sigma-Aldrich (Merck Group, Darmstadt, Germany).

### 4.2. Synthesis of Zn<sub>2</sub>SnO<sub>4</sub> Nanoparticles

To synthesize Zn<sub>2</sub>SnO<sub>4</sub> nanoparticles, 2.9749 g of zinc nitrate (Zn(NO<sub>3</sub>)<sub>2</sub>·6H<sub>2</sub>O) and 0.7 mL of tin tetrachloride (SnCl<sub>4</sub>) were employed as sources of zinc and tin, respectively. Each chemical was dissolved separately in 50 mL of distilled water to form two clear solutions. These solutions were then combined and mixed at 300 rpm for 2 h. A solution of 4 g of sodium hydroxide (NaOH) dissolved in 50 mL of distilled water was added dropwise to the Zn-Sn mixture while undergoing magnetic stirring. The mixture was maintained under stirring for an additional 2 h at 200 rpm before being transferred to SynthWAVE equipment for further processing. The synthesized composite powder was washed three times with ethanol and distilled water, followed by centrifugation at 6000 rpm/~3000 × g for 5 min to eliminate any residuals. The precipitate was then calcined at 100 °C for 7 h.

#### 4.3. Synthesis of $Zn_2SnO_4@SiO_2$ Nanoparticles

To create a  $SiO_2$  shell around the zinc stannate particles, the Stöber method was employed using the pre-synthesized  $Zn_2SnO_4$  powder. A quantity of 0.285 g of  $Zn_2SnO_4$  nanoparticles was mixed with 10 mL of ethanol and 10 mL of distilled water, and the mixture was subjected to magnetic stirring for 10 min. Simultaneously, 1 mL of aqueous ammonia solution was prepared and added dropwise to the nanoparticle suspension. Following this, 1.5 mL of tetraethyl orthosilicate (TEOS) was introduced into the mixture, which was then left under continuous magnetic stirring for 36 h. The resulting compound was washed three times with ethanol and distilled water, with each cycle followed by centrifugation at 6000 rpm/ $\sim 3000 \times g$  for 5 min. The final precipitate was heated in an oven at 140 °C for 10 h to complete the process.

#### 4.4. Synthesis of $Zn_2SnO_4@SiO_2@5-FU$ Nanoparticles

The  $SiO_2$ -coated  $Zn_2SnO_4$  nanoparticles were subsequently functionalized with 5-Fluorouracil (5-FU) using hydrogen and Van der Waals interactions. To achieve this, 5-FU was dissolved in ethanol and subjected to ultrasonic treatment at 80 °C, for 10 min, at 100 W. The 5-FU was added in a 1% mass ratio relative to the  $Zn_2SnO_4@SiO_2$  nanoparticles. The mixture was then manually ground with a mortar and pestle until the ethanol had completely evaporated. This surface modification ensured the controlled and stable attachment of 5-FU molecules to the  $SiO_2$ -coated  $Zn_2SnO_4$  surface. The modified nanoparticles demonstrated enhanced biocompatibility, greater bioavailability, and increased efficacy in targeting cancer cells.

#### 4.5. Characterization Methods

##### 4.5.1. X-Ray Diffraction (XRD)

The crystallinity and crystal parameters investigation of the  $Zn_2SnO_4$ ,  $Zn_2SnO_4@SiO_2$ , and  $Zn_2SnO_4@SiO_2@5-FU$  was performed through an X-ray diffraction technique, using in this sense a PANalytical Empyrean model diffractometer purchased from PANalytical, Almelo, the Netherlands, equipped with a hybrid monochromator (2xGe 220) on the incident side and parallel plate collimator mounted on PIXcel 3D detector on the diffracted side. Grazing Incidence X-ray Diffraction (GIXRD) measurements were performed at room temperature, with an angle of incidence  $\omega = 0.5^\circ$  for Bragg angle values of  $2\theta$  between  $10^\circ$  and  $80^\circ$ , using Cu  $K\alpha$  radiation with  $\lambda = 1.5406 \text{ \AA}$  (40 mA and 45 kV).

##### 4.5.2. Scanning Electron Microscopy (SEM)

To examine the morphological characteristics of  $Zn_2SnO_4$ ,  $Zn_2SnO_4@SiO_2$ , and  $Zn_2SnO_4@SiO_2@5-FU$  nanoparticles, a Scanning Electron Microscopy (SEM) analysis was conducted. The samples were mounted on carbon-coated slides and placed in the analysis chamber of an Inspect F50 scanning electron microscope, acquired from Thermo Fisher—FEI (Eindhoven, The Netherlands). The images were obtained by capturing the secondary electron emission and electron beam scattering, using an accelerating energy of 30 keV.

##### 4.5.3. Dynamic Light Scattering (DLS)

Dynamic Light Scattering (DLS) measurements were conducted using a DelsaMax Pro device (Backman Coulter, Brea, CA, USA), equipped with a 532 nm laser. The nanoparticle powders were dispersed in ultrapure water at room temperature. To ensure optimal dispersion, all samples underwent ultrasonic treatment for 10 min in an ultrasonic bath prior to measurement.

#### 4.5.4. Fourier Transform Infrared Spectroscopy (FTIR)

Fourier Transform Infrared (FTIR) analysis was conducted to identify the functional compositional groups present in the samples. A Thermo iN10-MX FTIR spectrometer (Thermo Fischer Scientific, Waltham, MA, USA), equipped with a ZnSe crystal, was used for the measurements. The spectra were collected over a range of 4000 to 400  $\text{cm}^{-1}$ . The instrument was sourced from Thermo Fisher Scientific, Waltham, MA, USA.

#### 4.5.5. Antimicrobial Assay

The minimum inhibitory concentration (MIC) was determined using the microdilution method. This procedure was conducted in 96-well plates using Trypticase Soy Broth (TSB) liquid medium or a simple broth, with a final volume of 150  $\mu\text{L}$  per well. Serial binary dilutions were prepared from each test solution, with concentrations ranging from 2 mg/mL to 0.0078 mg/mL (i.e., 2, 1, 0.5, 0.25, 0.125, 0.0625, 0.0156, and 0.0078 mg/mL). After preparing the appropriate dilutions, 15  $\mu\text{L}$  of a microbial suspension with a standard density (0.5 McFarland for bacteria, 1.0 McFarland for yeasts) was added to each well. The same dilution series was prepared for the solvent used to create the test dilutions, such as DMSO.

The 96-well plates were incubated at 37 °C for 24 h in a humid chamber. Results were assessed through macroscopic observation and/or by spectrophotometric measurement at 600 nm. For spectrophotometric analysis, 100  $\mu\text{L}$  of each sample was transferred to a new 96-well plate for accurate readings.

#### 4.5.6. In Vitro Cytotoxicity

The antitumor potential of  $\text{Zn}_2\text{SnO}_4$ ,  $\text{Zn}_2\text{SnO}_4@\text{SiO}_2$ , and  $\text{Zn}_2\text{SnO}_4@\text{SiO}_2@5\text{-FU}$  powders was assessed using the A-431 human epidermoid carcinoma cell line. Cells were maintained in Dulbecco's Modified Eagle's Medium (DMEM), supplemented with 10% fetal bovine serum (FBS) and 1% antibiotic-antifungal mixture, under standard conditions of 37 °C and 5%  $\text{CO}_2$ .

For treatment application, the cells were detached from the culture surface using enzymatic-chemical trypsin/EDTA detachment, counted using a hemocytometer, and seeded at a density of  $1 \times 10^4$  cells per well in sterile 96-well plates. The cells were incubated for 24 h under standard conditions before applying treatments. A 2 mg/mL stock solution was prepared in a complete culture medium for each of the three tested powders and then sterilized by passing through a 0.22  $\mu\text{m}$  syringe filter. This stock solution was used to prepare treatment solutions with concentrations of 1 mg/mL, 500  $\mu\text{g}/\text{mL}$ , 250  $\mu\text{g}/\text{mL}$ , 125  $\mu\text{g}/\text{mL}$ , 75  $\mu\text{g}/\text{mL}$ , 37.5  $\mu\text{g}/\text{mL}$  and 1.5  $\mu\text{g}/\text{mL}$ . The culture medium was removed from the wells and replaced with the treatment solutions, while the fresh culture medium was used as a control. After 24 h of treatment, two key assessments were conducted.

The MTT assay was used to quantify cell viability. This colorimetric assay measures cell viability and proliferation based on the ability of metabolically active cells to reduce yellow tetrazolium salt (MTT) into purple formazan crystals, a process that occurs at the mitochondrial level via NADH-dependent oxidoreductases. After 24 h of treatment, the culture medium was aspirated from the cell monolayers and replaced with a freshly prepared MTT solution, dissolved in a serum-free medium to a final concentration of 1 mg/mL. The plates were incubated for 4 h under standard conditions. The MTT solution was then removed, and the resulting formazan crystals were dissolved in isopropanol. The optical density (OD) of the solutions was measured at a wavelength of 550 nm using a FlexStation III multimode plate reader (Molecular Devices, San Jose, CA, USA). Statistical analysis was conducted with GraphPad Prism V9 software using an ANOVA test with Bonferroni

correction. Data were presented as the mean of three biological replicates  $\pm$  standard deviation, with a statistical significance threshold of  $p < 0.05$ .

The Live/Dead assay was used to investigate cell viability and cellular organization under the influence of the treatments. This qualitative method allows for the simultaneous identification of live and dead cells using calcein and ethidium bromide (EtBr). The assay assesses intracellular esterase activity and plasma membrane integrity. Calcein AM, a nonfluorescent compound, penetrates viable cell membranes and is converted by intracellular esterases into calcein, which fluoresces green. EtBr only enters cells with damaged membranes and binds to nucleic acids, emitting a red fluorescence. The Live/Dead Viability Cytotoxicity Kit for mammalian cells (Invitrogen, Thermo Fischer Scientific, Waltham, MA, USA) was employed, with the staining solution prepared by diluting the kit components in serum-free medium to a final concentration of 2  $\mu$ M calcein AM and 4  $\mu$ M EtBr. After 15 min of incubation at room temperature in the dark, the samples were examined under an Olympus IX73 inverted fluorescence microscope. Images were captured and processed using CellSense Imaging Software V 8.0.2 (Olympus, Tokyo, Japan).

## 5. Conclusions

This study highlights that  $\text{Zn}_2\text{SnO}_4@\text{SiO}_2@5\text{-FU}$  nanoparticles are a promising multifunctional additive for bone fillers in dental maxillofacial reconstruction. The synthesis process effectively retained the crystallinity of  $\text{Zn}_2\text{SnO}_4$  even after  $\text{SiO}_2$  coating and 5-FU functionalization, as confirmed by X-ray diffraction analysis. The  $\text{SiO}_2$  layer significantly enhanced the stability of the nanoparticles in aqueous environments, while 5-FU improved biocompatibility and exhibited effective antimicrobial and antitumor properties. Antibacterial tests indicated strong inhibitory activity against Gram-positive bacteria, making these nanoparticles suitable for infection prevention in clinical settings. Additionally, cytotoxicity studies on the A-431 human epidermoid carcinoma cell line demonstrated a dose-dependent reduction in cell viability, highlighting the potential of these nanoparticles for targeted cancer therapy. The successful inhibition of biofilm formation further supports the utility of  $\text{Zn}_2\text{SnO}_4@\text{SiO}_2@5\text{-FU}$  in preventing bacterial colonization. These results suggest that  $\text{Zn}_2\text{SnO}_4@\text{SiO}_2@5\text{-FU}$  nanoparticles could serve as a valuable component in bone fillers, enhancing their therapeutic and antimicrobial performance in dental and maxillofacial reconstruction applications. Future research should explore *in vivo* efficacy to confirm these findings and optimize clinical outcomes.

**Author Contributions:** Data curation, A.-G.N., F.C.B., P.C.B., A.M.P., A.M.G. and G.-A.C.; formal analysis, A.M.G.R., A.G.B., A.C.B., A.-G.N., A.M.H., A.H., F.C.B., A.M.P. and G.-A.C.; investigation, A.M.G.R., A.G.B., A.C.B., A.-G.N., A.M.H., A.H. and F.C.B.; methodology, A.C.B. and A.M.G.; validation, A.C.B., F.C.B., P.C.B., A.M.P., A.M.G. and G.-A.C.; writing—original draft, A.M.G.R., A.G.B., A.C.B., A.-G.N., A.M.H., A.H., F.C.B., P.C.B., A.M.P., A.M.G. and G.-A.C.; writing—review and editing, A.M.G.R., A.G.B., A.C.B., A.-G.N., P.C.B. and A.M.G. All authors have read and agreed to the published version of the manuscript.

**Funding:** This research received no external funding.

**Institutional Review Board Statement:** Not applicable.

**Informed Consent Statement:** Not applicable.

**Data Availability Statement:** The original contributions presented in this study are included in the article. Further inquiries can be directed to the corresponding author.

**Conflicts of Interest:** The authors declare no conflicts of interest.

## References

1. Salem, S.S.; Hammad, E.N.; Mohamed, A.A.; El-DougDoug, W. A Comprehensive Review of Nanomaterials: Types, Synthesis, Characterization, and Applications. *Biointerface Res. Appl. Chem.* **2023**, *13*, 41. [[CrossRef](#)]
2. Ngo, H.X.; Bai, Y.; Sha, J.; Ishizuka, S.; Toda, E.; Osako, R.; Kato, A.; Morioka, R.; Ramanathan, M.; Tatsumi, H.; et al. A Narrative Review of u-HA/PLLA, a Bioactive Resorbable Reconstruction Material: Applications in Oral and Maxillofacial Surgery. *Materials* **2021**, *15*, 150. [[CrossRef](#)] [[PubMed](#)]
3. Li, N.; Wang, J.; Feng, G.; Liu, Y.; Shi, Y.; Wang, Y.; Chen, L. Advances in biomaterials for oral-maxillofacial bone regeneration: Spotlight on periodontal and alveolar bone strategies. *Regen. Biomater.* **2024**, *11*, rbae078. [[CrossRef](#)]
4. Zhao, R.; Yang, R.; Cooper, P.R.; Khurshid, Z.; Shavandi, A.; Ratnayake, J. Bone Grafts and Substitutes in Dentistry: A Review of Current Trends and Developments. *Molecules* **2021**, *26*, 3007. [[CrossRef](#)]
5. Gkika, D.A.; Maliaris, G.; Vordos, N.; Mitropoulos, A.C.; Kyzas, G.Z. Cost Profile of 3D Printing Using Biomaterials on a Lab Scale. *Biointerface Res. Appl. Chem.* **2023**, *13*, 21. [[CrossRef](#)]
6. Salaam, A.; Thakur, S.; Prajapati, B.K.; Davala, K.; Rajalakshmi, B.; Nijhawan, G.; Saha, A. Bio Materials, Biocompatibility & its Advancements in Medical. In Proceedings of the E3S Web of Conferences, Bangkok, Thailand, 8–9 August 2024; p. 01092.
7. Tan, B.; Tang, Q.; Zhong, Y.; Wei, Y.; He, L.; Wu, Y.; Wu, J.; Liao, J. Biomaterial-based strategies for maxillofacial tumour therapy and bone defect regeneration. *Int. J. Oral Sci.* **2021**, *13*, 9. [[CrossRef](#)]
8. Ding, Q.; Cui, J.; Shen, H.; He, C.; Wang, X.; Shen, S.G.F.; Lin, K. Advances of nanomaterial applications in oral and maxillofacial tissue regeneration and disease treatment. *Wiley Interdiscip. Rev. Nanomed. Nanobiotechnol.* **2020**, *13*, e1669. [[CrossRef](#)]
9. Beenken, K.E.; Campbell, M.J.; Ramirez, A.M.; Alghazali, K.; Walker, C.M.; Jackson, B.; Griffin, C.; King, W.; Bourdo, S.E.; Rifkin, R.; et al. Evaluation of a bone filler scaffold for local antibiotic delivery to prevent *Staphylococcus aureus* infection in a contaminated bone defect. *Sci. Rep.* **2021**, *11*, 10254. [[CrossRef](#)]
10. Raj, M.; Singh, M.; Kumar, V.; Yadav, M.; Sherawat, N.; Sharma, A.K.; Sharma, V.; Sharma, J. An Updated Overview of Nanostructured Silver as a Novel Class of Biomedical Agent. *Lett. Appl. NanoBioScience* **2024**, *13*, 198.
11. Mollaamin, F.; Monajjemi, M.; Naeimi, M.; Zare, K. Investigation on Controlling Therapy of Bone Skeletal and Marrow Cancer: A Biophysical Chemistry and Molecular Dynamic Study of Bisphosphonates Interaction with Bone Structures. *Biointerface Res. Appl. Chem.* **2023**, *13*, 1–21. [[CrossRef](#)]
12. Cheah, C.W.; Al-Namnam, N.M.; Lau, M.N.; Lim, G.S.; Raman, R.; Fairbairn, P.; Ngeow, W.C. Synthetic Material for Bone, Periodontal, and Dental Tissue Regeneration: Where Are We Now, and Where Are We Heading Next? *Materials* **2021**, *14*, 6123. [[CrossRef](#)] [[PubMed](#)]
13. de Oliveira, I.R.; Dos Santos Gonçalves, I.; Wallace Dos Santos, K.; Lança, M.C.; Vieira, T.; Carvalho Silva, J.; Cengiz, I.F.; Reis, R.L.; Oliveira, J.M.; Miranda Ribeiro Borges, J.P. Biocomposite Macrospheres Based on Strontium-Bioactive Glass for Application as Bone Fillers. *ACS Mater. Au* **2023**, *3*, 646–658. [[CrossRef](#)]
14. Bauso, L.V.; La Fauci, V.; Longo, C.; Calabrese, G. Bone Tissue Engineering and Nanotechnology: A Promising Combination for Bone Regeneration. *Biology* **2024**, *13*, 237. [[CrossRef](#)]
15. Li, X.; Wang, Y.; Huang, D.; Jiang, Z.; He, Z.; Luo, M.; Lei, J.; Xiao, Y. Nanomaterials Modulating the Fate of Dental-Derived Mesenchymal Stem Cells Involved in Oral Tissue Reconstruction: A Systematic Review. *Int. J. Nanomed.* **2023**, *18*, 5377–5406. [[CrossRef](#)] [[PubMed](#)]
16. Tanaka, M.; Izumiya, M.; Haniu, H.; Ueda, K.; Ma, C.; Ueshiba, K.; Ideta, H.; Sobajima, A.; Uchiyama, S.; Takahashi, J.; et al. Current Methods in the Study of Nanomaterials for Bone Regeneration. *Nanomaterials* **2022**, *12*, 1195. [[CrossRef](#)] [[PubMed](#)]
17. Mahmoudi, H. Therapeutic utility of nanomaterial in oral and maxillofacial tissue regeneration. *Nanomed. Res. J.* **2022**, *7*, 312–319. [[CrossRef](#)]
18. Babuska, V.; Kasi, P.B.; Chocholata, P.; Wiesnerova, L.; Dvorakova, J.; Vrzakova, R.; Neklionova, A.; Landsmann, L.; Kulda, V. Nanomaterials in Bone Regeneration. *Appl. Sci.* **2022**, *12*, 6793. [[CrossRef](#)]
19. Huang, X.; Lou, Y.; Duan, Y.; Liu, H.; Tian, J.; Shen, Y.; Wei, X. Biomaterial scaffolds in maxillofacial bone tissue engineering: A review of recent advances. *Bioact. Mater.* **2024**, *33*, 129–156. [[CrossRef](#)] [[PubMed](#)]
20. Pandimurugan, A.R.; Sankaranarayanan, K. Antibacterial and photocatalytic activity of ZnO, SnO<sub>2</sub> and Zn<sub>2</sub>SnO<sub>4</sub> nanoparticles prepared by Microwave assisted method. *Mater. Technol.* **2022**, *37*, 717–727. [[CrossRef](#)]
21. Alghamdi, A.I.; Ababutain, I.M.; Alonizan, N.H.; Hjiri, M.; Hammad, A.H.; Zerrad, B.; Aida, M.S. Antibacterial activity of stannate M<sub>2</sub>SnO<sub>4</sub> (M = Co, Cu, Mg, Ni and Zn) nanoparticles prepared by hydrothermal. *Appl. Nanosci.* **2022**, *12*, 1601–1611. [[CrossRef](#)]
22. Hameed, R.K.; Al-Jawad, S.M.H.; Imran, N.J. Investigation of Structural, Morphological, and Optical Properties of Fe and Co/Fe Dual-Doping Zn<sub>2</sub>SnO<sub>4</sub> Nanoparticles Synthesized by Hydrothermal Method for Biomedical Application. *Plasmonics* **2024**, 1–15. [[CrossRef](#)]

23. Dillip, G.R.; Nagajyothi, P.C.; Ramaraghavulu, R.; Banerjee, A.N.; Reddy, B.V.; Joo, S.W. Synthesis of crystalline zinc hydroxystannate and its thermally driven amorphization and recrystallization into zinc orthostannate and their phase-dependent cytotoxicity evaluation. *Mater. Chem. Phys.* **2020**, *248*, 122946. [[CrossRef](#)]
24. Anjum, S.; Hashim, M.; Malik, S.A.; Khan, M.; Lorenzo, J.M.; Abbasi, B.H.; Hano, C. Recent Advances in Zinc Oxide Nanoparticles (ZnO NPs) for Cancer Diagnosis, Target Drug Delivery, and Treatment. *Cancers* **2021**, *13*, 4570. [[CrossRef](#)] [[PubMed](#)]
25. Pandimurugan, A.R.; Prasath, G.V.; Usha, K.S.; Vivekanandan, J.; Karthikeyan, C.; Sankaranarayanan, K.; Ravi, G. Synthesis, properties and antibacterial activity of Ca doped Zn<sub>2</sub>SnO<sub>4</sub> nanoparticles by microwave assisted method. *Appl. Phys. A* **2023**, *129*, 154. [[CrossRef](#)]
26. Davodiroknabadi, A. Modification of polyester fabrics with Zn<sub>2</sub>SnO<sub>4</sub> nanorods for superior self-cleaning, UV-protection and antibacterial performance. *J. Text. Inst.* **2023**, *114*, 1091–1098. [[CrossRef](#)]
27. Kamo, A.; Ates Sonmezoglu, O.; Sonmezoglu, S. Unraveling the Effects of Strain-Induced Defect Engineering on the Visible-Light-Driven Photodynamic Performance of Zn<sub>2</sub>SnO<sub>4</sub> Nanoparticles Modified by Larger Barium Cations. *ACS Appl. Bio Mater.* **2024**, *7*, 8656–8670. [[CrossRef](#)] [[PubMed](#)]
28. Lakshmi, Y.V.B.; Swapna, P.; Babu, B.K.; Rao, Y.S. Morphology and Anti-microbial Studies of Zinc Stannate Nanoparticles Constructed via Green Synthesis Approach. *Lett. Appl. NanoBioSci.* **2023**, *12*, 138. [[CrossRef](#)]
29. Sun, M.; Yin, C.; Yan, Z.; Wei, Z.-J.; Zhang, Z.; Wang, W.; Yuan, Z. Energy recruitment via lanthanide-chelate to boost the persistent luminescence of nanophosphor for contrast-enhanced tumor navigation. *Chem. Eng. J.* **2023**, *468*, 143814. [[CrossRef](#)]
30. Tan, P.; Li, Y.-H.; Liu, X.-Q.; Jiang, Y.; Sun, L.-B. Core-Shell AgCl@SiO<sub>2</sub> Nanoparticles: Ag(I)-Based Antibacterial Materials with Enhanced Stability. *ACS Sustain. Chem. Eng.* **2016**, *4*, 3268–3275. [[CrossRef](#)]
31. Gao, M. Synthesis and Characterization of Superparamagnetic Fe<sub>3</sub>O<sub>4</sub>@SiO<sub>2</sub> Core-Shell Composite Nanoparticles. *World J. Condens. Matter Phys.* **2011**, *1*, 49–54. [[CrossRef](#)]
32. Dharmalingam, N.; Vaseekaran, M.; Mariappan, R. Design, Cytotoxicity, and Tumor Targeted Drug Delivery of 5-Fluorouracil Encapsulated in pH-Sensitive Co-polymers GG-g-P (HEMA) Conjugate Riboflavin Thin-Film. *Biointerface Res. Appl. Chem.* **2023**, *13*, 285. [[CrossRef](#)]
33. Niazy, A.A.; Alrashed, M.M.; Lambarte, R.N.A.; Niazy, A.A. 5-Fluorouracil Inhibits Bacterial Growth and Reduces Biofilm in Addition to Having Synergetic Effects with Gentamicin Against *Pseudomonas aeruginosa*. *Microorganisms* **2024**, *12*, 2257. [[CrossRef](#)]
34. Da'i, M.; Wikantyasning, E.R.; Maryati; Wahyuni, A.S.; Mirzaei, M. A Titanium-Enhanced Boron Nitride Fullerene for the Drug Delivery of 5-Fluorouracil Anticancer: DFT Study. *Biointerface Res. Appl. Chem.* **2023**, *13*, 434.
35. Dharmalingam, N.; Arumugasamy, V.; Mariappan, R.; Vijayakumar, K.K.; Harshavardhan, S. Development of Targeted Magnetic Bentonite Nanocarrier for the Delivery of 5-Fluorouracil. *Biointerface Res. Appl. Chem.* **2023**, *13*, 491.
36. Niavol, S.S.; Khatibani, A.B.; Hashemi Karouei, S.F.; Hejazi Juybari, S.A.; Moghaddam, H.M. Mesoporous Zn<sub>2</sub>SnO<sub>4</sub> for efficient sensing of ethylene glycol vapor. *Mater. Chem. Phys.* **2023**, *303*, 127799. [[CrossRef](#)]
37. Silvestri, S.; Stefanello, N.; da Silveira Salla, J.; Foletto, E.L. Photocatalytic properties of Zn<sub>2</sub>SnO<sub>4</sub> powders prepared by different modified hydrothermal routes. *Res. Chem. Intermed.* **2019**, *45*, 4299–4313. [[CrossRef](#)]
38. Nivethaa, E.A.K.; Dhanavel, S.; Rebekah, A.; Narayanan, V.; Stephen, A. A comparative study of 5-Fluorouracil release from chitosan/silver and chitosan/silver/MWCNT nanocomposites and their cytotoxicity towards MCF-7. *Mater. Sci. Eng. C Mater. Biol. Appl.* **2016**, *66*, 244–250. [[CrossRef](#)]
39. Eshghi Esfahani, R.; Zahedi, P.; Zarghami, R. 5-Fluorouracil-loaded poly(vinyl alcohol)/chitosan blend nanofibers: Morphology, drug release and cell culture studies. *Iran. Polym. J.* **2020**, *30*, 3. [[CrossRef](#)]
40. Zuo, J.; Quan, Y.; Li, J.; Li, Y.; Song, D.; Li, X.; Wang, Y.; Yi, L.; Wang, Y. Tackling Antibiotic Resistance: Exploring 5-Fluorouracil as a Promising Antimicrobial Strategy for the Treatment of *Streptococcus suis* Infection. *Animals* **2024**, *14*, 1286. [[CrossRef](#)]
41. Anzellini, S.; Diaz-Anichtchenko, D.; Sanchez-Martin, J.; Turnbull, R.; Radescu, S.; Mujica, A.; Muñoz, A.; Ferrari, S.; Pampillo, L.; Bilovol, V.; et al. High-Pressure Behavior of Ca<sub>2</sub>SnO<sub>4</sub>, Sr<sub>2</sub>SnO<sub>4</sub>, and Zn<sub>2</sub>SnO<sub>4</sub>. *J. Phys. Chem. C* **2024**, *128*, 1357–1367. [[CrossRef](#)]
42. Zhang, M.; Song, H.; Yang, S.; Zhang, Y.; Tian, Y.; Wang, Y.; Liu, D. Deciphering the Antibacterial Mechanisms of 5-Fluorouracil in *Escherichia coli* through Biochemical and Transcriptomic Analyses. *Antibiotics* **2024**, *13*, 528. [[CrossRef](#)]
43. Xia, Y.; Wang, H.; Li, Y.; Fu, C. Engineered bone cement trigger bone defect regeneration. *Front. Mater.* **2022**, *9*, 929618. [[CrossRef](#)]
44. Jeong, J.; Kim, J.H.; Shim, J.H.; Hwang, N.S.; Heo, C.Y. Bioactive calcium phosphate materials and applications in bone regeneration. *Biomater. Res.* **2019**, *23*, 4. [[CrossRef](#)] [[PubMed](#)]
45. Youness, R.A.; Tag El-deen, D.M.; Taha, M.A. A Review on Calcium Silicate Ceramics: Properties, Limitations, and Solutions for Their Use in Biomedical Applications. *Silicon* **2023**, *15*, 2493–2505. [[CrossRef](#)]
46. Balhaddad, A.A.; Garcia, I.M.; Mokeem, L.; Alsahafi, R.; Collares, F.M.; Sampaio de Melo, M.A. Metal Oxide Nanoparticles and Nanotubes: Ultrasmall Nanostructures to Engineer Antibacterial and Improved Dental Adhesives and Composites. *Bioengineering* **2021**, *8*, 146. [[CrossRef](#)]

47. Shineh, G.; Mobaraki, M.; Afzali, E.; Alakija, F.; Velisdeh, Z.; Mills, D. Antimicrobial Metal and Metal Oxide Nanoparticles in Bone Tissue Repair. *Biomed. Mater. Devices* **2024**, *2*, 1–24. [[CrossRef](#)]
48. Zhang, S.; Lin, L.; Huang, X.; Lu, Y.-G.; Zheng, D.-L.; Feng, Y. Antimicrobial properties of metal nanoparticles and their oxide materials and their applications in oral biology. *J. Nanomater.* **2022**, *2022*, 2063265. [[CrossRef](#)]
49. Nguyen, N.H.; Lu, Z.; Elbourne, A.; Vasilev, K.; Roohani, I.; Zreiqat, H.; Truong, V.K. Engineering antibacterial bioceramics: Design principles and mechanisms of action. *Mater. Today Bio* **2024**, *26*, 101069. [[CrossRef](#)] [[PubMed](#)]
50. Nicolae, C.-L.; Pîrvulescu, D.-C.; Niculescu, A.-G.; Rădulescu, M.; Grumezescu, A.M.; Croitoru, G.-A. An Overview of Nanotechnology in Dental Medicine. *J. Compos. Sci.* **2024**, *8*, 352. [[CrossRef](#)]
51. Lims, S.C.; Divya, S.; Manivannan, M.; Arumanayagam, T.; Robert, R.; Jose, M. Investigation of structural, temperature and frequency dependent dielectric behavior of Zn<sub>2</sub>SnO<sub>4</sub>@amorphous SiO<sub>2</sub> core shell nanocomposites. *Chem. Phys. Impact* **2024**, *8*, 100485. [[CrossRef](#)]
52. Salman, D.; Juzsakova, T.; Al-Mayyahi, M.A.; Ákos, R.; Mohsen, S.; Ibrahim, R.I.; Mohammed, H.D.; Abdullah, T.A.; Domokos, E.; Korim, T. Synthesis, Surface Modification and Characterization of Magnetic Fe<sub>3</sub>O<sub>4</sub>@SiO<sub>2</sub> Core-Shell Nanoparticles. *J. Phys. Conf. Ser.* **2021**, *1773*, 012039. [[CrossRef](#)]
53. Ding, C.; Guo, Z.; Xiong, J.; Wu, D.; Tao, Y.; Qin, Y.; Kong, Y. Rational design of a multi-responsive drug delivery platform based on SiO<sub>2</sub>@PPy@poly(acrylic acid-co-acrylamide). *React. Funct. Polym.* **2019**, *137*, 88–95. [[CrossRef](#)]
54. Zuo, J.; Quan, Y.; Li, Y.; Song, D.; Li, J.; Wang, Y.; Yi, L.; Wang, Y. Targeting ThyA: Investigating the mechanisms of 5-FU-induced inhibition of biofilm formation and virulence in *Streptococcus suis* through LuxS/AI-2 quorum sensing1. *J. Integr. Agric.* **2024**. [[CrossRef](#)]
55. Chen, P.-C.; Su, B.-C.; Ma, T.-L.; Hong, Y.C.; Chen, Y.-W.; Vo, T.T.T.; Wu, L.-Y.; Peng, T.-Y.; Wang, C.-S.; Lee, I.-T. Enhancement of Anticancer Effects by Combining 5-Fluorouracil with Refametinib in Human Oral Squamous Cell Carcinoma Cell Line. *Appl. Sci.* **2023**, *13*, 4340. [[CrossRef](#)]
56. Moodley, T.; Singh, M. Polymeric Mesoporous Silica Nanoparticles for Enhanced Delivery of 5-Fluorouracil In Vitro. *Pharmaceutics* **2019**, *11*, 288. [[CrossRef](#)] [[PubMed](#)]
57. Montoya, C.; Du, Y.; Gianforcaro, A.L.; Orrego, S.; Yang, M.; Lelkes, P.I. On the road to smart biomaterials for bone research: Definitions, concepts, advances, and outlook. *Bone Res.* **2021**, *9*, 12. [[CrossRef](#)] [[PubMed](#)]
58. Lin, C.-R.; Ivanova, O.S.; Petrov, D.A.; Sokolov, A.E.; Chen, Y.-Z.; Gerasimova, M.A.; Zharkov, S.M.; Tseng, Y.-T.; Shestakov, N.P.; Edelman, I.S. Amino-Functionalized Fe<sub>3</sub>O<sub>4</sub>@SiO<sub>2</sub> Core-Shell Magnetic Nanoparticles for Dye Adsorption. *Nanomaterials* **2021**, *11*, 2371. [[CrossRef](#)] [[PubMed](#)]

**Disclaimer/Publisher’s Note:** The statements, opinions and data contained in all publications are solely those of the individual author(s) and contributor(s) and not of MDPI and/or the editor(s). MDPI and/or the editor(s) disclaim responsibility for any injury to people or property resulting from any ideas, methods, instructions or products referred to in the content.